Supporting Information for Energy & Environmental Science

A robust chromium-iridium oxide catalyst for high-current-density acidic oxygen evolution in proton exchange membrane electrolyzers

Shiyu Ge[1], Ruikuan Xie[2], Bing Huang[3], Zhiyuan Zhang[1], Heming Liu[1], Xin Kang[1], Shuqi Hu[1], Shaohai Li[1], Yuting Luo[1], Qiangmin Yu[1*], Jingwei Wang[1], Guoliang Chai[2*], Lunhui Guan[3], Hui-Ming Cheng[4,5,6], and Bilu Liu[1*]

1. Shenzhen Geim Graphene Center, Tsinghua-Berkeley Shenzhen Institute & Institute of Materials Research, Tsinghua Shenzhen International Graduate School, Tsinghua University, Shenzhen 518055, P.R. China
2. State Key Laboratory of Structural Chemistry, Fujian Institute of Research on the Structure of Matter, Chinese Academy of Sciences, Fuzhou 350002, P.R. China
3. CAS Key Laboratory of Design and Assembly of Functional Nanostructures, Fujian Institute of Research on the Structure of Matter, Chinese Academy of Sciences, Fuzhou 350000, P.R. China
4. Shenyang National Laboratory for Materials Science, Institute of Metal Research, Chinese Academy of Sciences, Shenyang 110016, P.R. China
5. Faculty of Materials Science and Engineering, Institute of Technology for Carbon Neutrality, Shenzhen Institute of Advanced Technology, Chinese Academy of Sciences, Shenzhen 518055, P.R. China
6. Advanced Technology Institute, University of Surrey, Guildford, Surrey GU2 7XH, UK.

Corresponding authors

Email: bilu.liu@sz.tsinghua.edu.cn (B.L.)

yu.qiangmin@sz.tsinghua.edu.cn (Q.Y.)

g.chai@fjirsm.ac.cn (G.C.)

This file contains:

Experimental section

Figs. S1 to S31

Table S1-S8

References (1-76)

Experimental Section

Materials preparation: All chemicals were obtained from commercial suppliers in the analytical grade and used without further purification. First, porous chromium oxide was synthesized by a hydrothermal method[1] and calcination. The detailed process was as follows. Chromic nitrate (4 mmol, 99.95%, Macklin), terephthalic acid (4 mmol, 99%, Macklin), hydrochloric acid (4 mmol, 12 M) and deionized water (20 ml) were added to a Teflon-lined stainless steel autoclave with a piece of porous Ti foil and kept at 220 °C for 8 h in an explosion-proof heater. After the reaction, cooling and washing in hot ethanol (95% EtOH, 5% deionized water) at 80 °C for 8 h, the resulting product was dried at 150 °C in a vacuum condition for 12 h to remove the absorbed and coordinated water. Then Cr-based crystals on the porous Ti foil were calcined in air at 550 °C for 4 h to obtain porous chromium oxide grown on the porous Ti foil. Second, hexachloroiridium acid hydrate (39%, Macklin) was dissolved in deionized water to produce a 0.5 mmol L^{-1} solution, after which the foil was immersed in the H_2IrCl_6 solution (5 mL), so that the H_2IrCl_6 was uniformly dispersed in the pores of the chromium oxide. After drying, the foil was transferred to a muffle furnace and heated in air at 550 °C for 4 h. The XRD curve of this sample is shown in Fig. S4. After cooling, it underwent electrochemical oxidation at 50 mA cm^{-2} for 10 h, and the final porous Ti foil grown with chromium-iridium oxide was collected and denoted as the CrO_2-0.16IrO_2 electrocatalyst. The CrO_2-0.16IrO_2 electrocatalyst formed on the porous

Ti foil is used as the working electrode in the three-electrode system. The CrO_2-$0.16IrO_2$ electrocatalyst can also be synthesized in the form of powder and be used as the anode catalyst in the PEM electrolyzer. In the latter case, no substrate is used during the hydrothermal process. Other than that, the synthesis process of powder electrocatalyst is the same as the CrO_2-$0.16IrO_2$ electrocatalyst formed on Ti foil.

Materials characterization: Surface morphology and elemental analysis of the samples were performed by SEM (10kV, Zeiss, Germany). The phase structure of the samples was characterized by X-ray diffraction (XRD) on a D8 Advance Bruker diffractometer with Cu Kα ($\lambda = 1.54$ Å) radiation in the range of 20°-80° (2θ). Transmission electron microscopy (TEM) images were collected at a 200 kV electron acceleration voltage (FEI Tecnai F30, USA). Chemical analysis of the samples was conducted by X-ray photoelectron spectroscopy (XPS) on a PHI 5000 VersaProbe II spectrometer (Al Kα X-rays). Raman spectra were recorded on commercial Raman spectroscope (Horiba HR Evolution) by using a 532 nm laser as excitation light. X-ray absorption spectroscopy (XAS) spectra at the Ir L-edge were collected at the BL11B beamline of the Shanghai Synchrotron Radiation Facility (SSRF). 220 mA of beam current of the storage ring was applied in a top-up mode. The incident photons were monochromatized by a Si (111) double-crystal monochromator, with an energy resolution $\Delta E/E \approx 1.4\times10^{-4}$. The spot size at the sample was ≈200 μm × 250 μm (H × V). The resulting spectra were recorded in the fluorescence mode using a four-element silicon drift detector (SDD, Vortex ME-4). All spectra were collected under ambient conditions in the transition mode. The L_3-edge of Pt foil (edge energy: 11,564 eV) was measured for energy calibration. The Cr and Ir contents were determined by ICP-OES (SpectroArcos II MV, USA).

Electrochemical measurements: All the electrochemical measurements were conducted by using a VMP300 electrochemical workstation (Biologic. Comp, France) in a 0.5 M H_2SO_4 electrolyte. A standard three-electrode cell was established, using a piece of Pt foil as the counter electrode, a saturated Ag/AgCl as the reference electrode,

and the CrO_2-0.16IrO_2 electrocatalyst formed on the Ti foil as the working electrode. We used a salt bridge to reduce the distance between the working electrode and the reference electrode. Before tests on the electrochemical workstation, the acid electrolyte was purged with N_2 gas (99.999%) for 30 minutes to exclude oxygen. We used a reversible hydrogen electrode (RHE) to calibrate all of the collected potentials in the 0.5 M H_2SO_4 electrolyte. All the potentials were converted using the following equation: E (RHE) = E (Ag/AgCl) + 0.224 V. All the electrochemical tests were conducted using the same three-electrode cell and measurement parameters. Linear sweep voltammetry (LSV) curves were collected at a scan rate of 2.0 mV s^{-1}, typically between 1.0 and 2.0 V with an 85% *iR* correction. Electrochemical impedance spectroscopy (EIS) was performed at 1.50 V with frequencies from 1 MHz to 0.1 Hz, and the corresponding results were presented in the form of Nyquist plot with a representative equivalent electrical circuit fitted by ZView software. Chronopotentiometric (CP) measurements were made at a constant current density of 1,000 mA cm^{-2} for up to 100 h. For the stability test in Fig. 3e, the loading amount of commercial IrO_2 catalyst is 2.0 mg cm^{-2}. The TOF calculations of the CrO_2-0.16IrO_2 electrocatalyst are as follows.

$$TOF = N_{O2} / N_{Ir}, \qquad (S1)$$

where N_{O2} is the number of oxygen turnovers, N_{Ir} is the number of active Ir sites.

N_{O2} = (j mA cm^{-2}) × (A cm^2) × (1 C s^{-1}/1000 mA) × (1 mol e^-/96485 C) × (1 mol O_2/4 mol e-) × 6.02 × 10^{23} mol^{-1}.

N_{Ir} = (0.14 × (50 × 10^{-6} g × 6.02 × 10^{23} mol^{-1}) / molecular weight of CrO_2-0.16IrO_2. Therefore, TOF (CrO_2-0.16IrO_2) = 0.88 s^{-1} at 1.53 V vs RHE.

Computational methods: All the density functional theory (DFT) calculations were carried out by the Vienna Ab-initio Simulation Package (VASP)[2-5], and the projector augmented plane wave pseudopotentials from VASP library were used for the elements involved (PAW_PBE Ir, Cr, O, H)[6]. The generalized gradient approximation (GGA) within the Perdew, Burke, and Ernzerhof was used for the exchange correlation potential[7]. The GGA+U method is employed to calculate the onsite Coulomb

correlation for Cr-3d and Ir-5d electrons. The Coulomb repulsion energy U and exchange energy J for Cr-3d states are chosen to be 3 and 0.87 eV, respectively[8]. While for Ir-5d states, U and J are set to be 2 and 0 eV, respectively[9]. The atomic structure of the CrO_2-0.16IrO_2 electrocatalyst calculated in this study is shown in Fig. 4a. A vacuum region of greater than 15 Å was added along the direction normal to the slab plane to avoid the interaction between periodic supercells. The bottom layers were fixed during the structural relaxation. The electron wave function was expanded in plane waves and the cutoff energy was set to 750 eV. Monkhorst-Pack meshes of (3 × 3 × 1) were used for the Brillouin zone of the slab[10]. The energy convergence criterion and geometry relaxation were set to 1.0×10^{-4} eV and 0.01 eV $Å^{-1}$, respectively. Van de Waals interactions was considered using the approach of Grimme as implanted in VASP[11]. The adsorption energy of OER intermediate is calculated as[12]:

$$\Delta G = \Delta E_{Total} + \Delta E_{ZPE} - T\Delta S + \Delta G_s \qquad (S2)$$

where ΔE_{Total} is the calculated total energy by DFT, ΔE_{ZPE} is zero-point energy, T is temperature, ΔS is entropy and ΔG_s is solvation energy.

The calculated OER electrochemical potential is defined as[13]:

$$U_{OER} = Max[\Delta G_i] / ne \qquad (S3)$$

where *n* is the number of electrons transferred for each electrochemical step, and *e* is the elementary change. Here, *n* is set to 1 for the one-electron transfer step. The meaning of the Max is to select the maximum value in the brackets. ΔG_i is the free energy change for each elementary step of the OER.

DEMS measurements. We have designed three steps of DEMS experiments using $H_2{}^{18}O$ and $H_2{}^{16}O$ as the supporting solution (0.5 M H_2SO_4). The first step is labelling ^{18}O on the electrocatalyst, the CrO_2-0.16IrO_2 electrocatalyst was subjected to 11 CV cycles (1.0-1.5 V vs. RHE) in the $H_2{}^{18}O$ electrolyte. The second step is washing. The CrO_2-0.16IrO_2 electrocatalyst was washed by abundant water ($H_2{}^{16}O$). Then at the third step, the electrocatalyst underwent 4 consecutive CV cycles (1.0-1.6 V vs. RHE). The CrO_2-0.16IrO_2 steadily produced $^{32}O_2$ at each cycle while $^{36}O_2$ was not detected.

Electrochemical measurements in the PEM electrolyzer. A Nafion 117 membrane (N117, Dupont) was sequentially washed by 5 wt% H_2O_2, 0.5 M H_2SO_4, and deionized water at 80 °C for 1 h, 1 h and 0.5 h, respectively. After cooling to room temperature, the treated membrane was preserved in a 0.5 M H_2SO_4 electrolyte. The membrane electrode assembly was prepared using Nafion 117 by the catalyst-coated membrane method with a geometric area of 2.0 cm^2. The cathode catalyst is commercial Pt/C electrocatalyst and the anode catalyst is the CrO_2-0.16IrO_2 electrocatalyst (powder). To prepare the anodic catalyst ink, 10 mg of the CrO_2-0.16IrO_2 electrocatalyst was suspended in a mixture of 940 μL isopropanol and 60 μL Nafion (5 wt%), and was sonicated for at least 1 h. To prepare the cathodic catalyst ink, 5 mg of the Pt/C electrocatalyst was suspended in a mixture of 940 μL isopropanol and 60 μL Nafion (5 wt%), and was also sonicated for at least 1 h. The mass loadings of Pt/C (20%) were 0.6 mg cm^{-2} for the cathode. The mass loadings of the CrO_2-0.16IrO_2 powder were 3 mg cm^{-2} for the anode, which means the mass loadings of Ir is 0.59 mg cm^{-2}. The PEM electrolyzer using a commercial IrO_2 electrocatalyst also had an anodic load mass of 3.0 mg cm^{-2}. The membrane with electrocatalysts coated, the anode gas diffusion layer (Ti mesh), and the cathode gas diffusion layer (carbon paper) were hot pressed together to establish the MEA under 130 °C with a pressure of 10 MPa for 3 min. During the test, both the anode and cathode plate were heated to 80 °C. Besides, a flow of water preheated to 80 °C at 100 mL min^{-1} was supplied to the anode side. The performance evaluation of the PEM electrolyzer using the CrO_2-0.16IrO_2 electrocatalyst was performed by a Gamry (Gamry Instruments) Interface 5000E device. Linear sweep voltammetry (LSV) curves were collected at a scan rate of 2.0 mV s^{-1}, typically between 1.2 and 2.0 V. Chronopotentiometric (CP) measurements were conducted at a constant current density of 1.0 A cm^{-2} for up to 100 h.

Calculations of the efficiency, total gas produced, and hydrogen production electricity cost of CrO_2-0.16IrO_2 electrocatalyst in PEM electrolyzers.

The power, efficiency, total gas produced, and hydrogen production cost were all calculated under the stability test current density (1 A cm^{-2}).

(i). Efficiency

Electrolyzer power = 1.63 V × 1 A cm^{-2} = 1.63 W cm^{-2}.

The lower heating value (LHV) of H_2 is applied to calculate the efficiencies of CrO_2-0.16IrO_2 electrocatalyst. LHV = 120 kJ kg^{-1}.

The H_2 production rate at 1.0 A cm^{-2} is 5.18 × 10^{-6} mol H_2 cm^{-2} s^{-1}.

H_2 power out = H_2 production rate × LHV = 1.25 W cm^{-2}.

Efficiency = H_2 power out / Electrolyzer power × 100%= 76.7%.

(ii). Electricity cost of hydrogen production

Mass of produced H_2 = H_2 production rate × electrolyzer area × Molar mass H_2 × Time = 7.3 g H_2.

The O_2 production rate at 1 A cm^{-2} is 2.59 × 10^{-6} mol O_2 cm^{-2} s^{-1}.

Mass of produced O_2 = O_2 production rate × Electrolyzer area × Molar mass O_2 × Time = 58.4 g O_2.

Energy consumption = Electrolyzer power / (H_2 production rate × Molar mass H_2) = 43.7 kW h/kg H_2.

Electricity cost (H_2/kg) = Energy consumption × Electricity bill = 43.7 kW h/kg H_2 × $ 0.02/kW h=$ 0.87 /kg H_2.

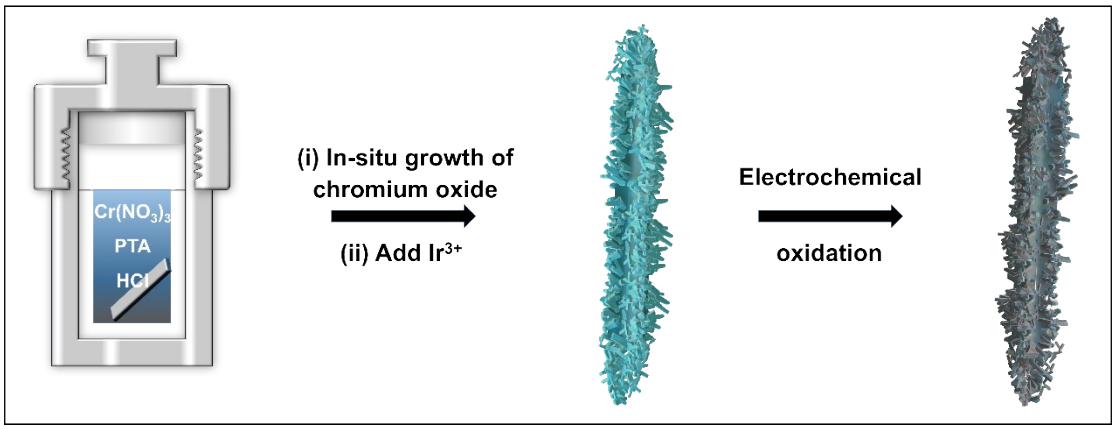

Figure S1. Schematic of the preparation of the CrO_2-0.16IrO_2 electrocatalyst.

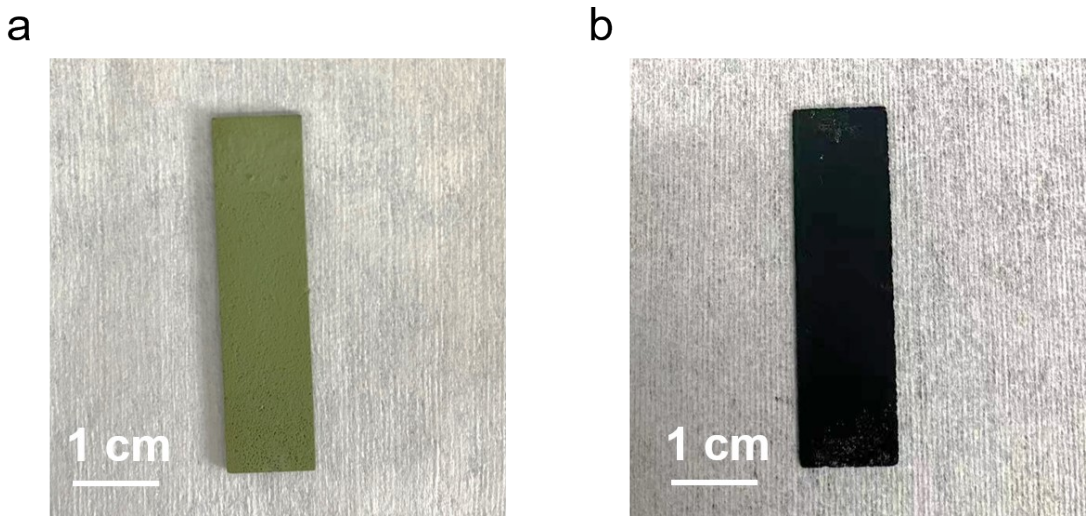

Figure S2. Optical photographs of **a** porous chromium oxide and **b** the CrO_2-0.16IrO_2 electrocatalyst.

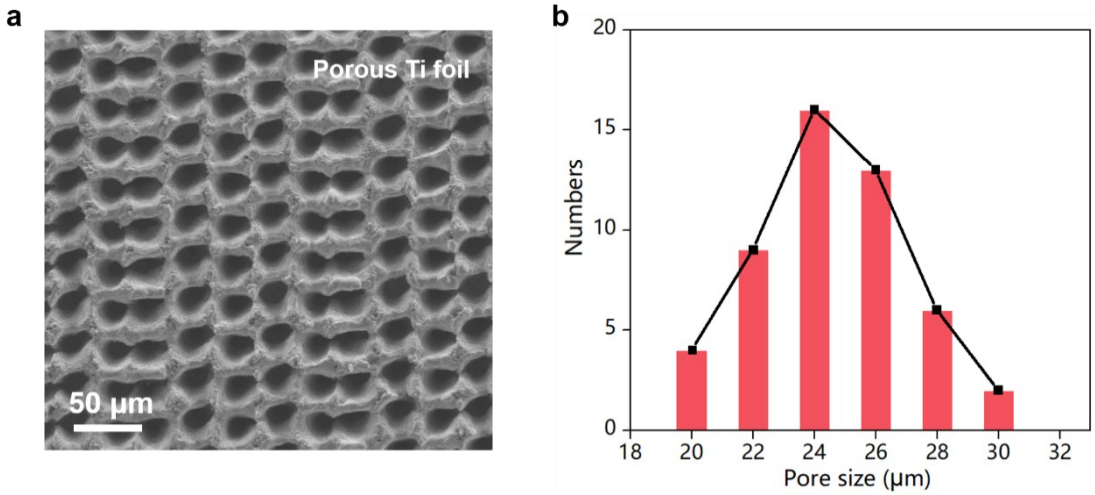

Figure S3. (a) SEM image of the porous Ti foil, (b) pore size of the porous Ti foil. The average pore size of porous Ti foil is 25 μm.

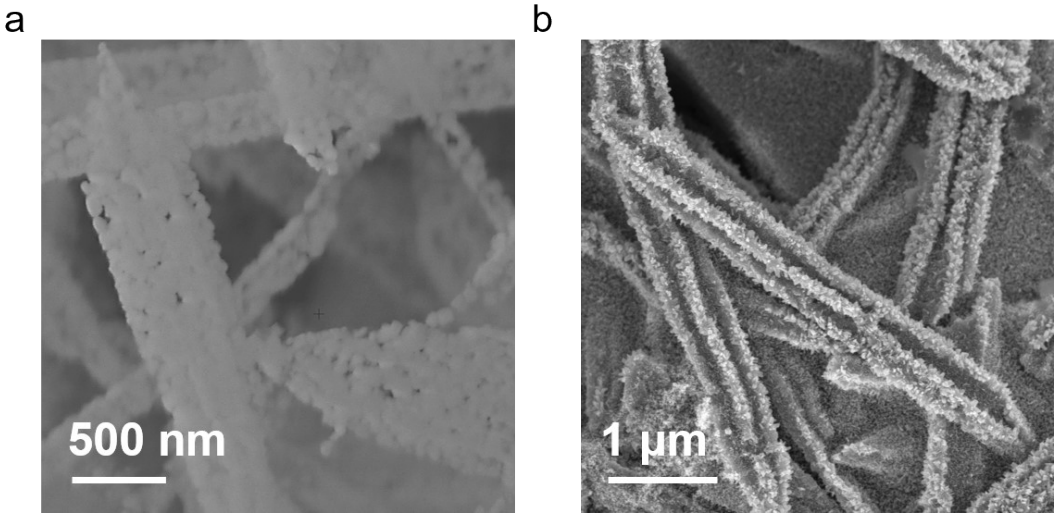

Figure S4. SEM images of **a** porous chromium oxide and **b** the CrO_2-0.16IrO_2 electrocatalyst.

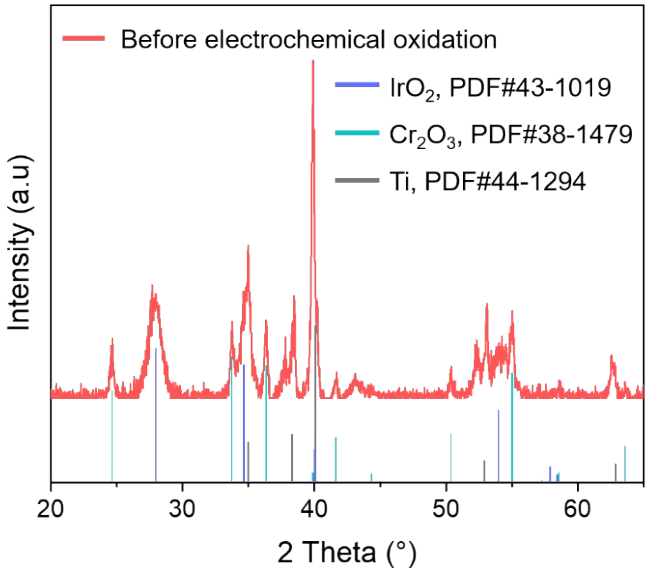

Figure S5. XRD pattern of the precursor of the CrO_2-0.16IrO_2 electrocatalyst, which is the sample before electrochemical oxidation.

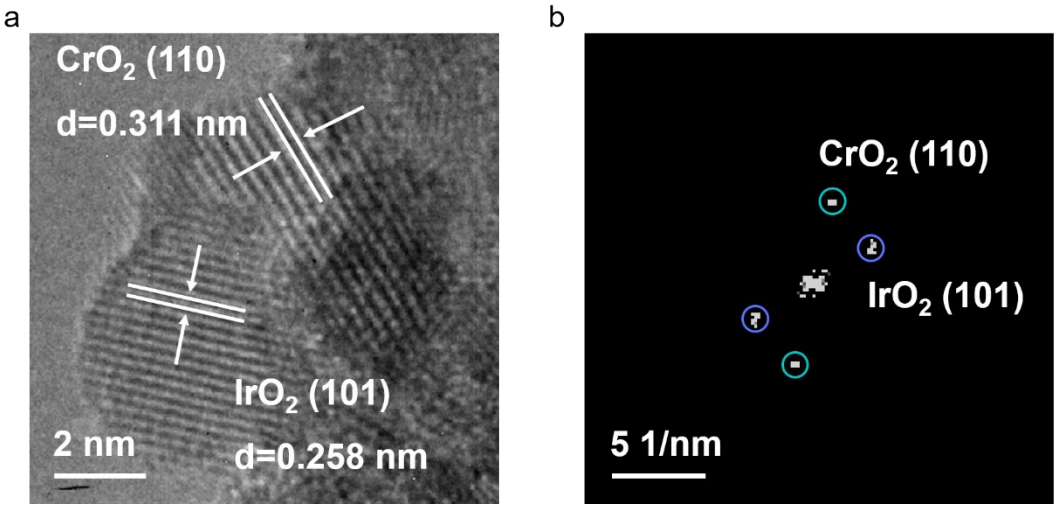

Figure S6. a High-resolution transmission electron microscopy (HRTEM) of the interface between CrO_2 (110) and IrO_2 (101) in CrO_2-0.16IrO_2. **b** the corresponding fast Fourier transform (FFT) of the interface between CrO_2 (110) and IrO_2 (101).

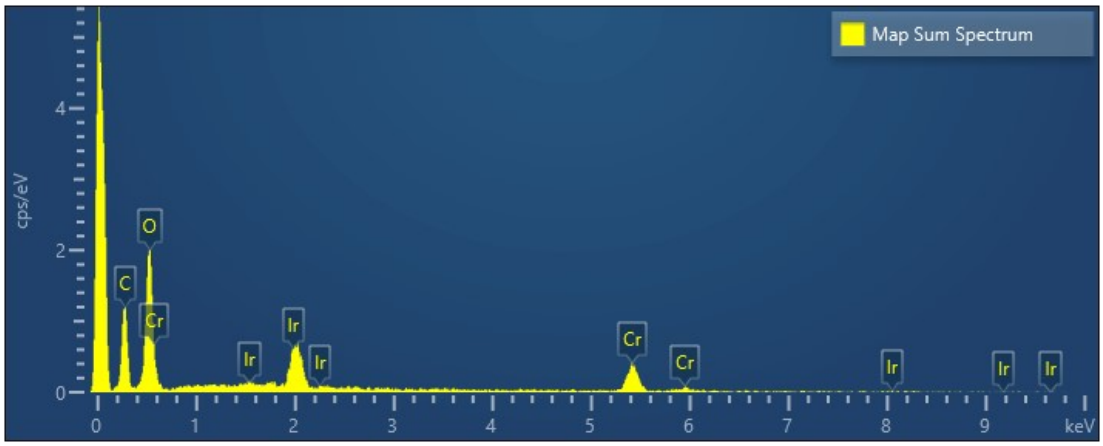

Element	Weight %	Weight % Sigma	Atomic %
Cr	31.94	6.29	14.22
Ir	19.67	2.14	2.37
O	20.44	2.04	29.56
C	27.95	2.78	53.85

Figure S7. EDS results of CrO_2-0.16IrO_2. The Cr/Ir ratio is consistent with ICP-OES.

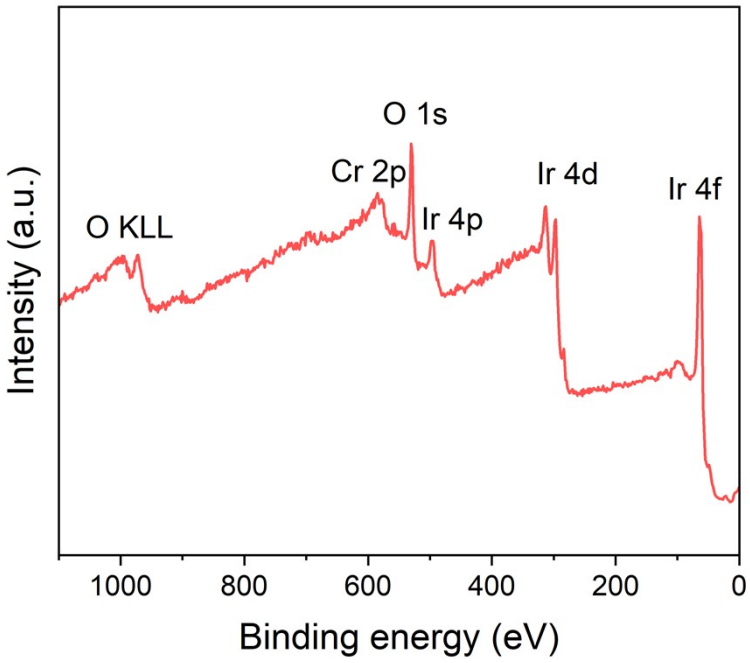

Figure S8. XPS survey spectrum of the CrO_2-0.16IrO_2 electrocatalyst.

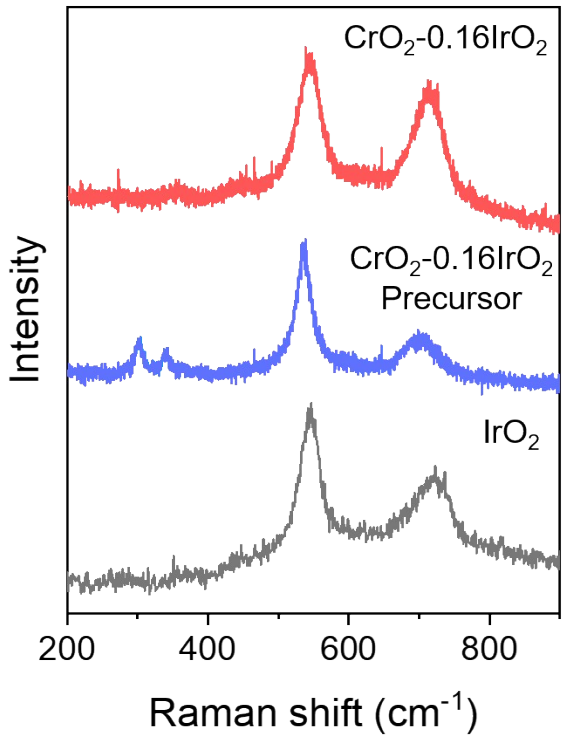

Figure S9. Raman spectra for IrO_2, the CrO_2-0.16IrO_2 precursor and the CrO_2-0.16IrO_2 electrocatalyst. The Raman spectrum of CrO_2-0.16IrO_2 shows typical Ir-O vibrational modes at approximately 547.1 cm^{-1} (E_g) and 712.2 cm^{-1} (the B_{2g} and A_{1g} overlapped) similar to those of the IrO_2 sample[14]. Raman shifts at 303.2 cm^{-1} and 348.9 cm^{-1} in the CrO_2-0.16IrO_2 precursor can be assigned to the Raman modes of Cr_2O_3 sample[15], while the disappearance of these two peaks in spectra for the CrO_2-0.16IrO_2 electrocatalyst is consistent with the XRD (Fig. 1b) and XPS results (Fig. 2a). Raman shifts (565.0 cm^{-1} and 683.0 cm^{-1}) of CrO_2 are close to those of IrO_2, and thus there are two main peaks in the CrO_2-0.16IrO_2 electrocatalyst[16].

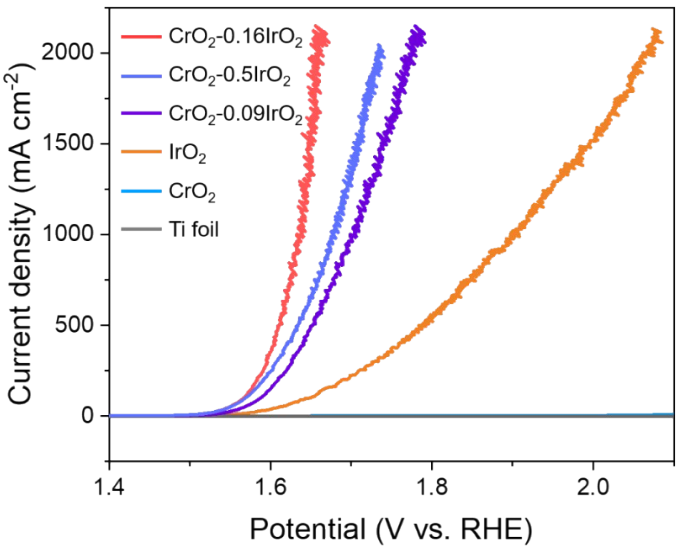

Figure S10. LSV curves of IrO_2, CrO_2, and chromium-iridium oxide electrocatalysts with different Cr/Ir ratios. We have investigated the activity of electrocatalysts with three different Cr/Ir ratios (2:1, 6:1, and 10:1). The CrO_2-0.16IrO_2 electrocatalyst with Cr/Ir ratio of 6/1 shows the best OER activity among all the three electrocatalysts.

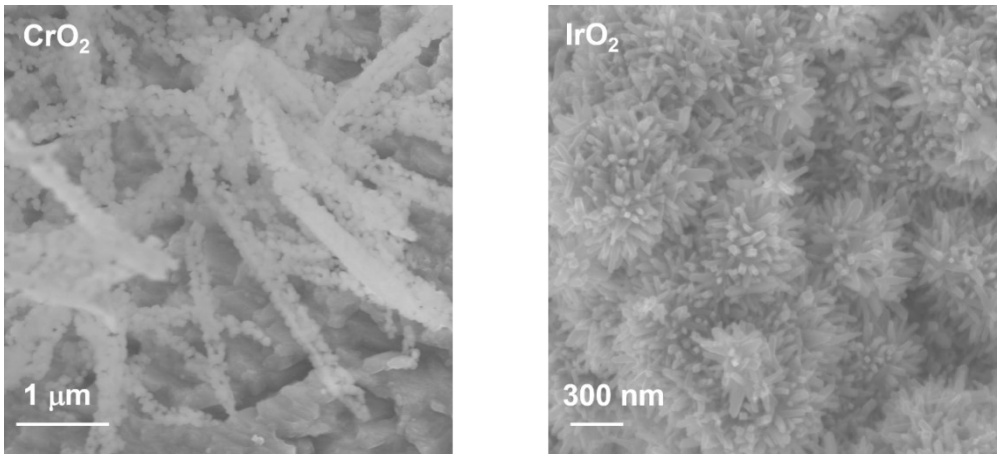

Figure S11. SEM images of (a) CrO_2 and (b) IrO_2 synthesized by the same template method.

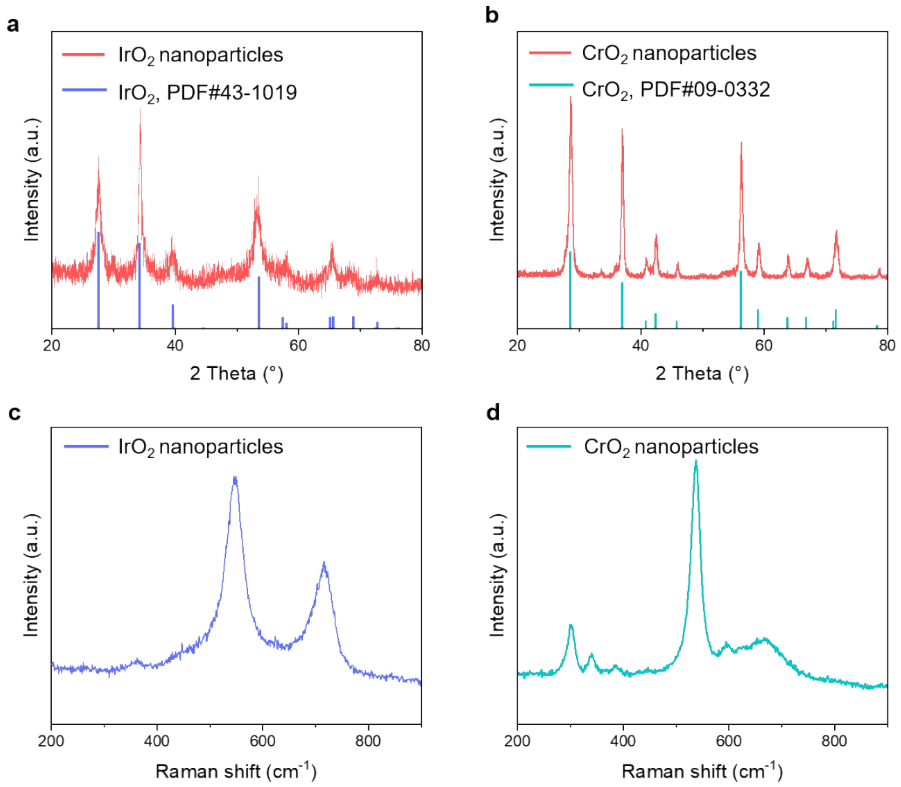

Figure S12. XRD patterns of (a) IrO_2 nanoparticles and (b) CrO_2 nanoparticles synthesized by the same template method. Raman spectra of (c) IrO_2 nanoparticles and (d) CrO_2 nanoparticles synthesized by the same template method. The laser wavelength is 532 nm.

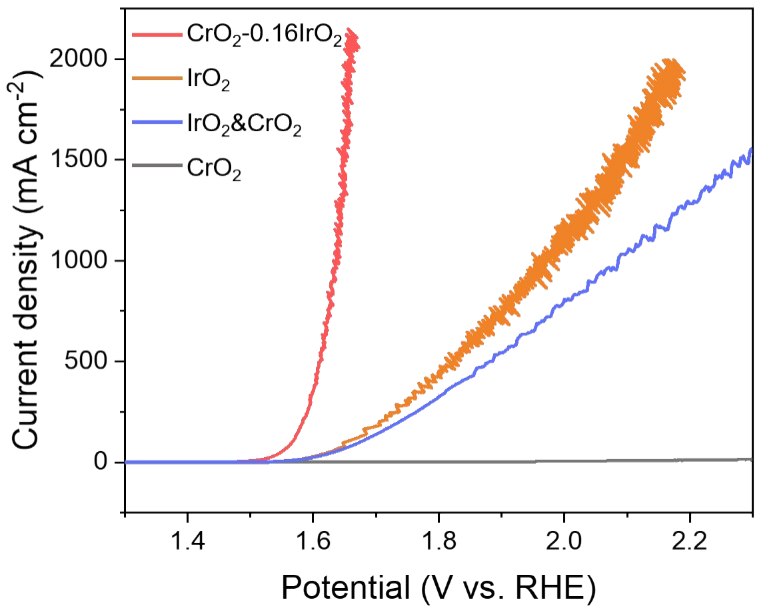

Figure S13. LSV curves of CrO_2, IrO_2, IrO_2&CrO_2, CrO_2-0.16IrO_2 electrocatalysts. We synthesized CrO_2, IrO_2, and CrO_2-0.16IrO_2 electrocatalysts based on the same template method and compared their OER activity. The CrO_2 synthesized by the same template method has negligible catalytic activity. The IrO_2 synthesized by the same template method has good activity and the overpotential at 2,000 mA cm^{-2} of IrO_2 electrocatalyst is 948 mV, which is much higher than that of the CrO_2-0.16IrO_2 electrocatalyst (425 mV). When we simply mixed IrO_2 and CrO_2 to make the IrO_2&CrO_2 catalyst, it shows lower activity than CrO_2-0.16IrO_2 with strong coupling interfaces, showing that the improved activity is related to the strong coupling interfaces formed in CrO_2-0.16IrO_2 electrocatalyst. Overall, to decrease the Ir usage and tune the electronic structure of IrO_2, we designed CrO_2-0.16IrO_2 electrocatalyst with excellent activity towards acidic OER.

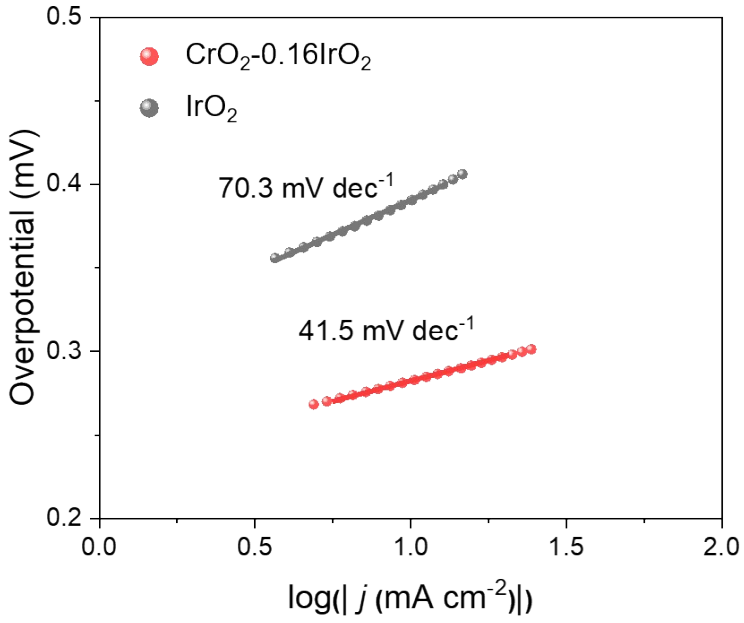

Figure S14. Tafel plots of CrO_2-0.16IrO_2 and IrO_2 electrocatalysts in a 0.5 M H_2SO_4 electrolyte.

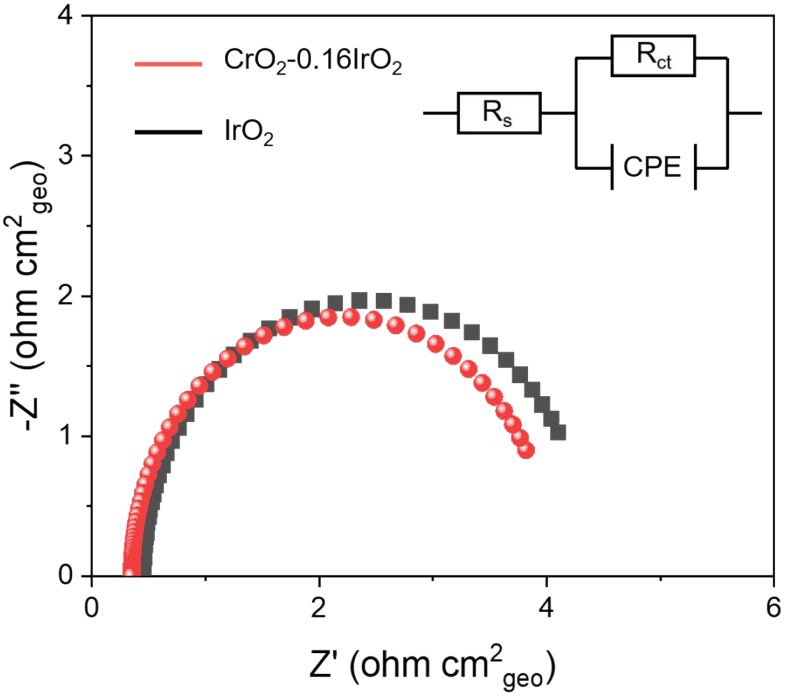

Figure S15. Electrochemical impedance spectra and fitted circuits of the CrO_2-0.16IrO_2 and IrO_2 electrocatalysts in a 0.5 M H_2SO_4 electrolyte.

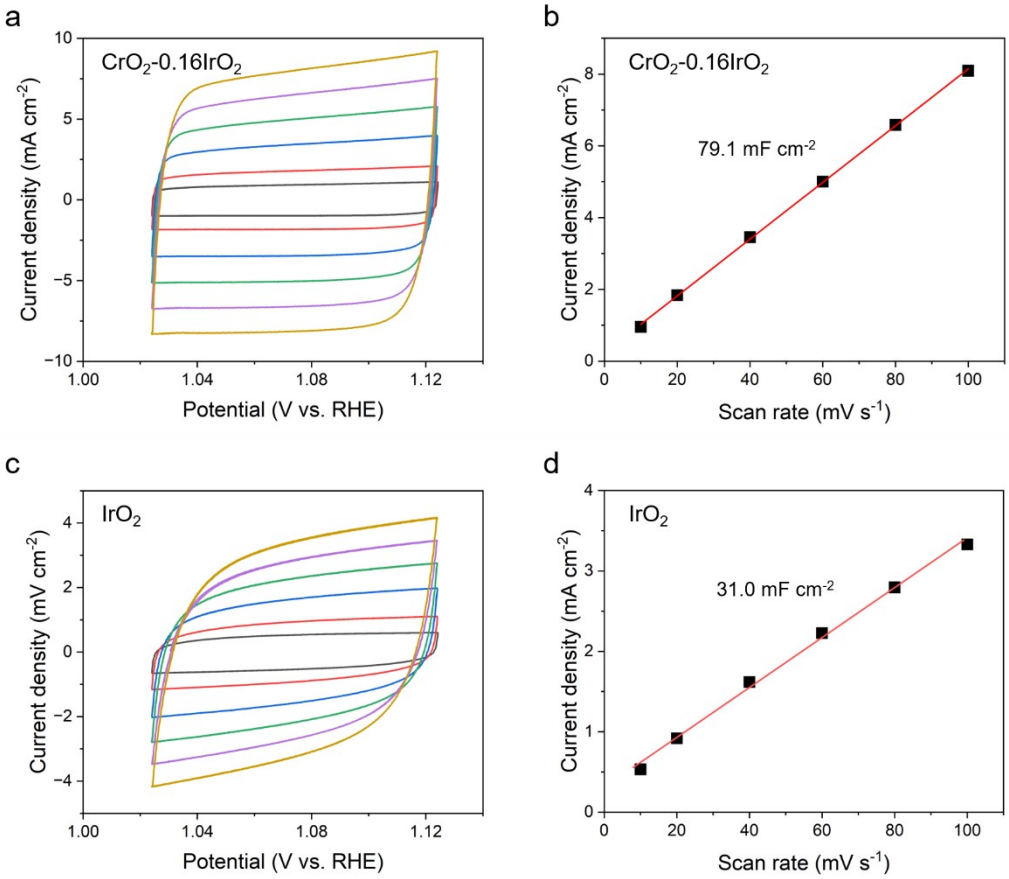

Figure S16. Double-layer capacitance of CrO_2-0.16IrO_2 and IrO_2 electrocatalysts in a 0.5 M H_2SO_4 electrolyte. **a** CV curves at different scan rates of CrO_2-0.16IrO_2. **b** Corresponding double-layer capacitance of CrO_2-0.16IrO_2. **c** CV curves at different scan rates of IrO_2 electrocatalyst. **d** Corresponding double-layer capacitance of CrO_2-0.16IrO_2. CV curves were obtained in a non-Faradaic region of the voltammogram at the following scan rate: 10, 20, 40, 60, 80, and 100 mV s^{-1}. The capacitive current was measured at 1.07 V against the scan rate. The corresponding C_{dl} values were estimated by linear fitting of the plots for CrO_2-0.16IrO_2 and IrO_2 electrocatalysts. ECSA = C_{dl} / C_s, while C_s is the specific capacitance[17]. The ECSA value of CrO_2-0.16IrO_2 is calculated to be 1,976.5, while that of IrO_2 is calculated to be 775.8. A higher ECSA indicates the exposure of more active sites in CrO_2-0.16IrO_2 than in IrO_2.

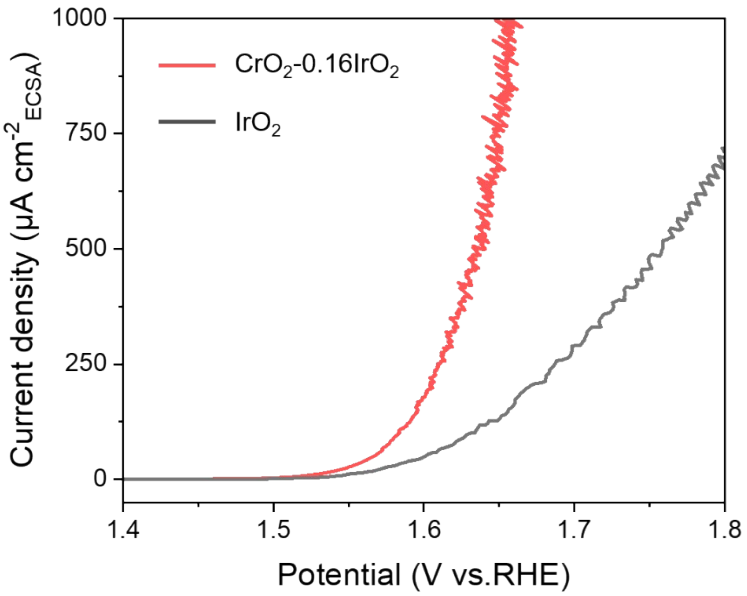

Figure S17. Polarization curves normalized by ECSA of CrO_2-0.16IrO_2 and IrO_2 electrocatalysts.

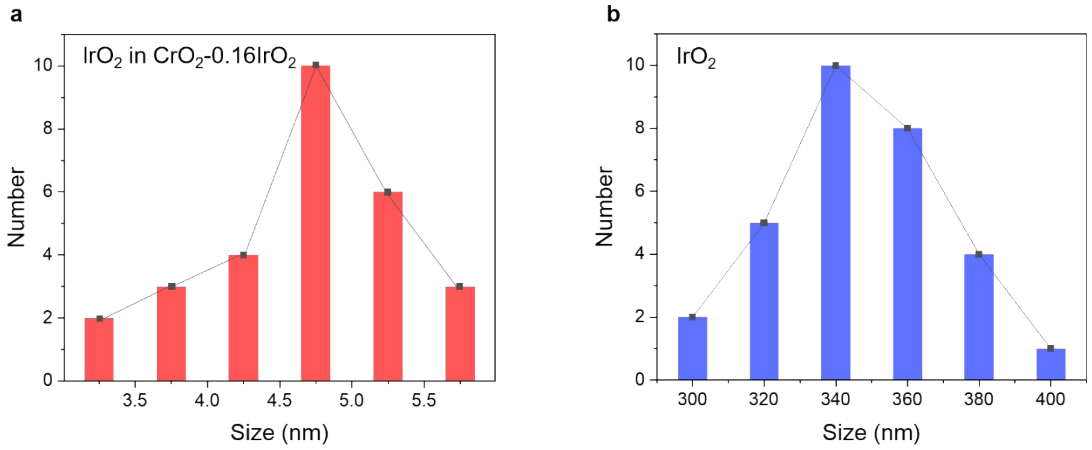

Figure S18. The particle size of the (a) IrO_2 in CrO_2-0.16IrO_2 electrocatalyst and (b) commercial IrO_2 electrocatalyst. The average particle size of IrO_2 in CrO_2-0.16IrO_2 electrocatalyst is about 4.4 nm. The average particle size of the commercial IrO_2 is about 346.7 nm.

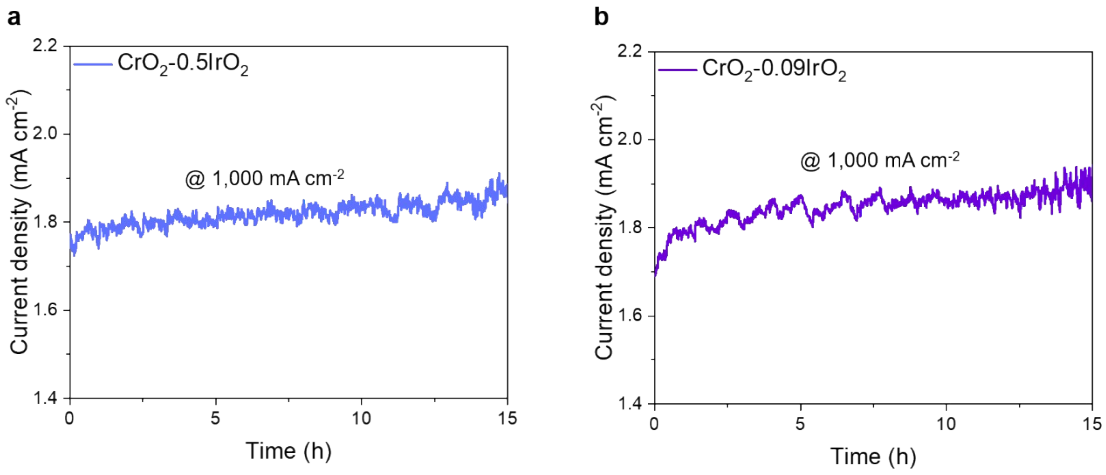

Figure S19. I-t curves of the (a) CrO_2-0.5IrO_2 and (b) CrO_2-0.09IrO_2 electrocatalysts at 1 A cm^{-2} in a 0.5 M H_2SO_4 electrolyte.

When operating at 1,000 mA cm^{-2}, CrO_2-0.5IrO_2 and CrO_2-0.09IrO_2 electrocatalysts deliver higher degradation rates compared with CrO_2-0.16IrO_2 electrocatalyst, suggesting that CrO_2-0.16IrO_2 electrocatalyst with Cr/Ir ratio of 6/1 also shows the best stability.

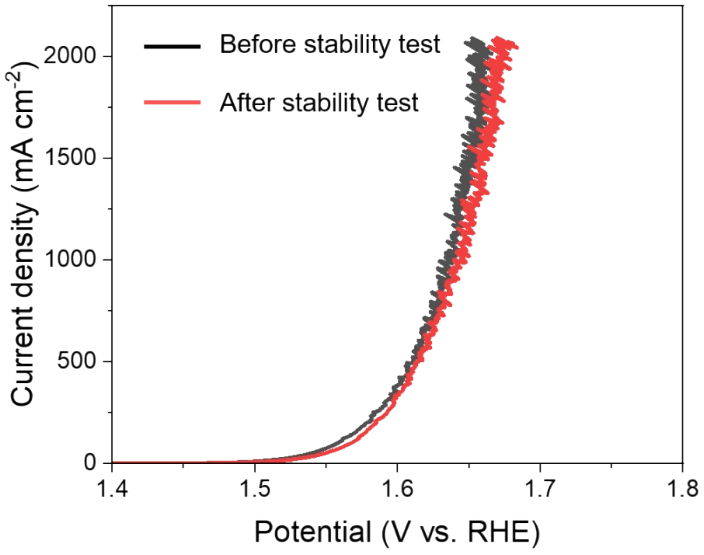

Figure S20. Polarization curves of the CrO_2-0.16IrO_2 electrocatalyst after a 100-h stability test in 0.5 M H_2SO_4 electrolyte. There is no obvious activity change after the stability test, suggesting the excellent durability of the CrO_2-0.16IrO_2 electrocatalyst.

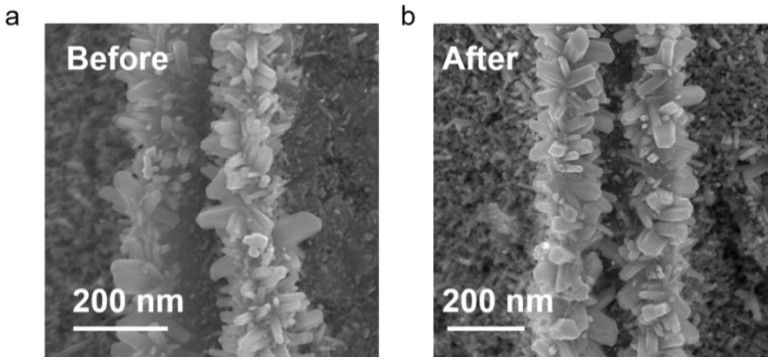

Figure S21. SEM images of the CrO_2-0.16IrO_2 electrocatalyst (a) before and (b) after the 100-h stability test.

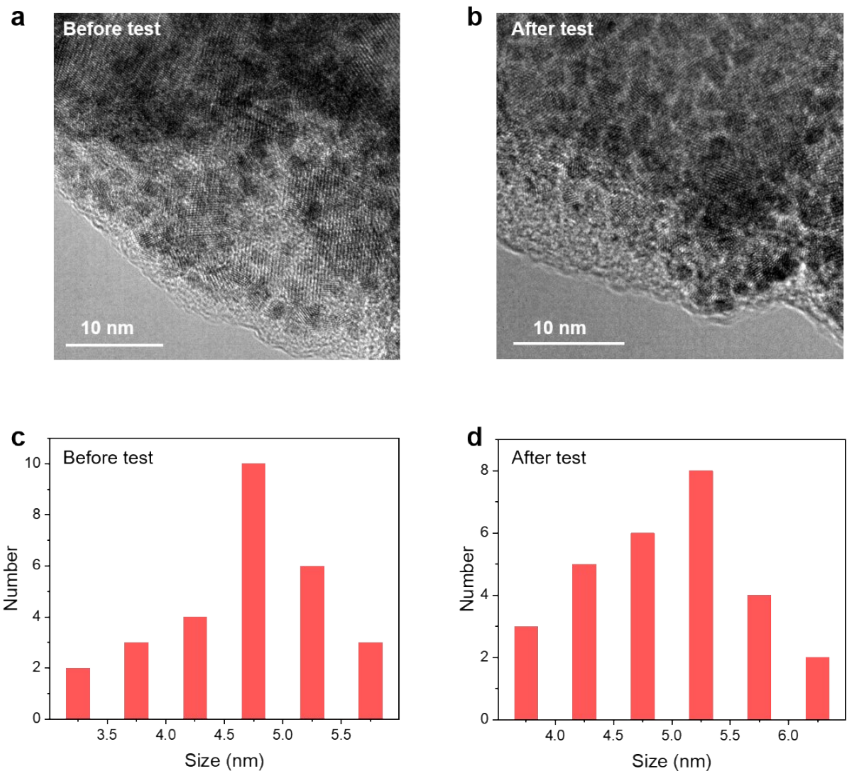

Figure S22. TEM images of the CrO_2-0.16IrO_2 (a) before and (b) after the 100-h stability test. The particle size of IrO_2 in the CrO_2-0.16IrO_2 electrocatalyst (c) before and (d) after the 100-h stability test. The average size of IrO_2 particles is about 4.4 nm before the stability test and about 4.7 nm after the stability test, respectively. The particle size increases a bit after the stability test because a few of the IrO_2 particles would aggregate after long-term OER. While the major structure mains well, which is consistent with the excellent stability of the CrO_2-0.16IrO_2 electrocatalyst.

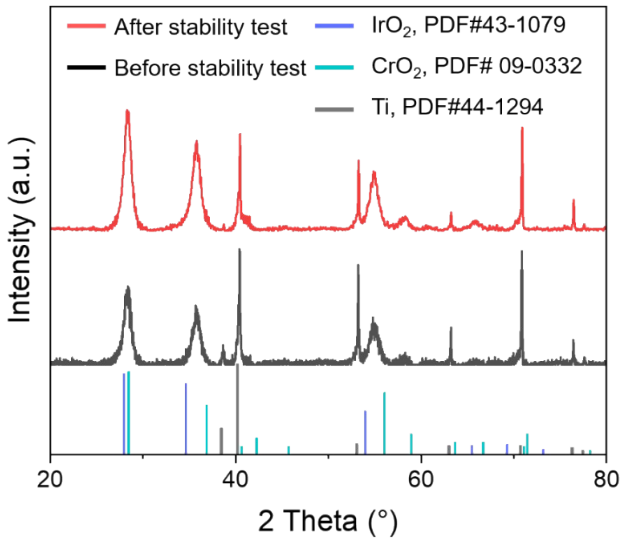

Figure S23. Comparison of XRD patterns of the CrO_2-0.16IrO_2 electrocatalyst before and after the 100-h stability test.

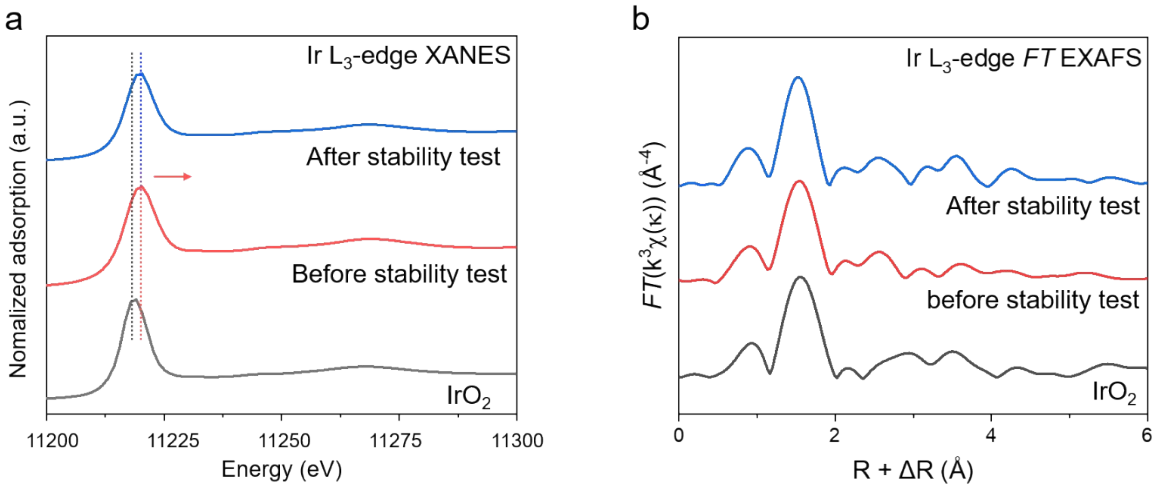

Figure S24. XANES and EXAFS spectra of the CrO_2-0.16IrO_2 electrocatalyst before and after the 100-h stability test.

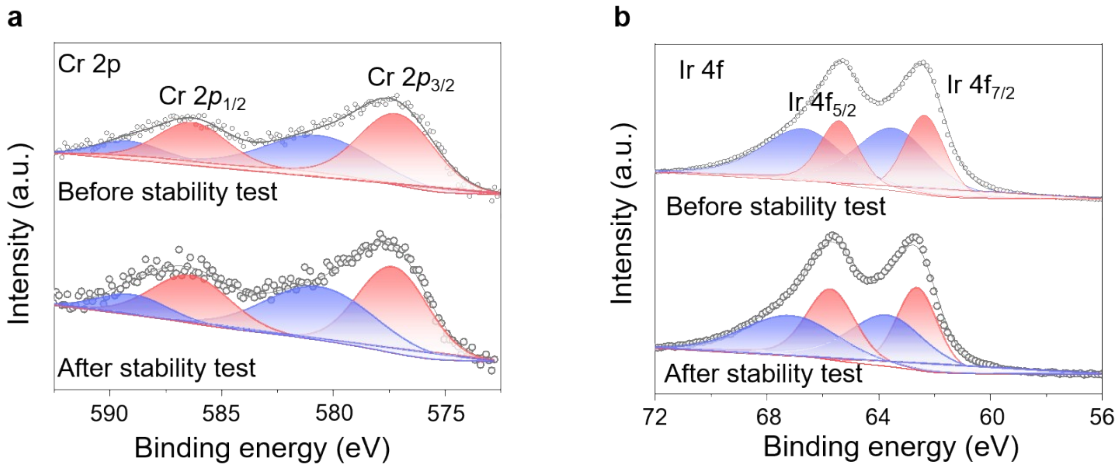

Figure S25. The comparison of XPS results before and after the 100-h stability test. (a) Cr 2*p* spectra of the CrO_2-0.16IrO_2 electrocatalyst, (b) Ir 4*f* spectra of the CrO_2-0.16IrO_2 electrocatalyst.

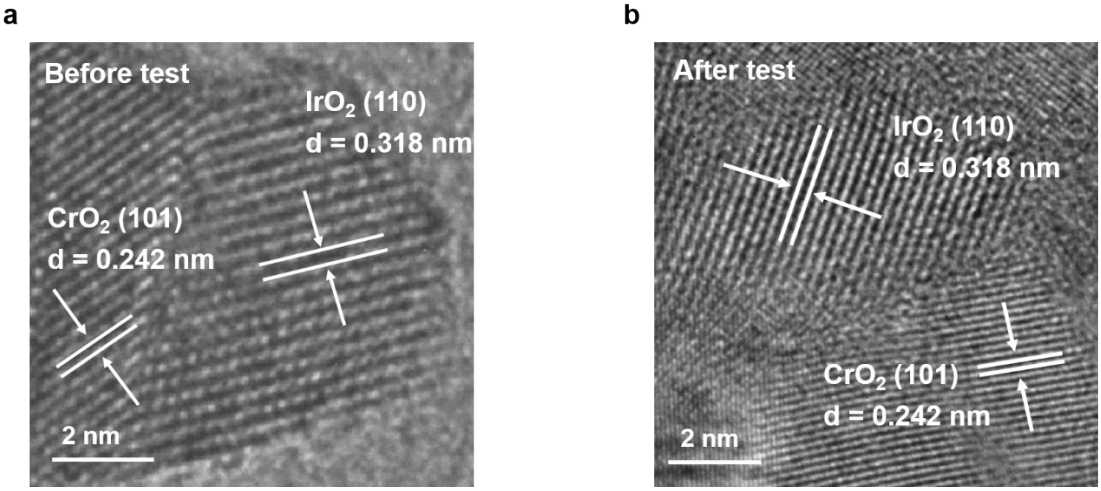

Figure S26. (a) High-resolution transmission electron microscopy (HRTEM) images of the CrO_2-0.16IrO_2 electrocatalyst (a) before the stability test, and (b) after the 100-h stability test.

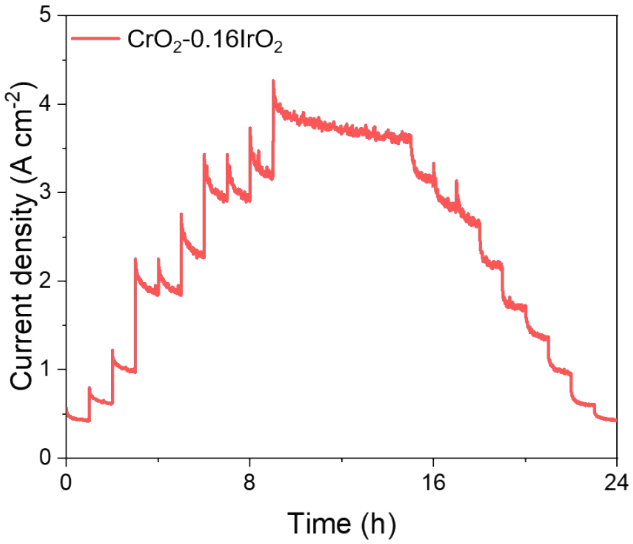

Figure S27. A simulation stability test of wind/solar-power with the potential in the range of 1.45-2.25 V.

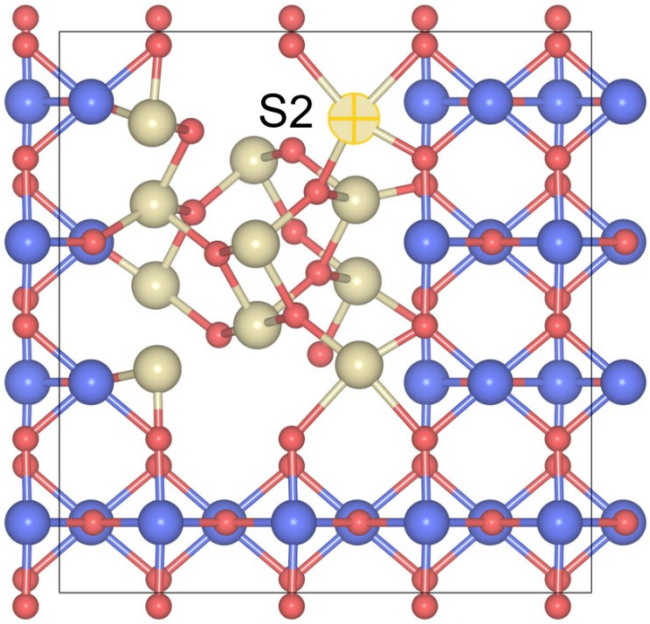

Figure S28. Simulated model of interface between CrO_2 (110) and IrO_2 (101) in the CrO_2-0.16IrO_2 electrocatalyst. Blue, gold, and red balls represent Cr, Ir, and O atoms, respectively.

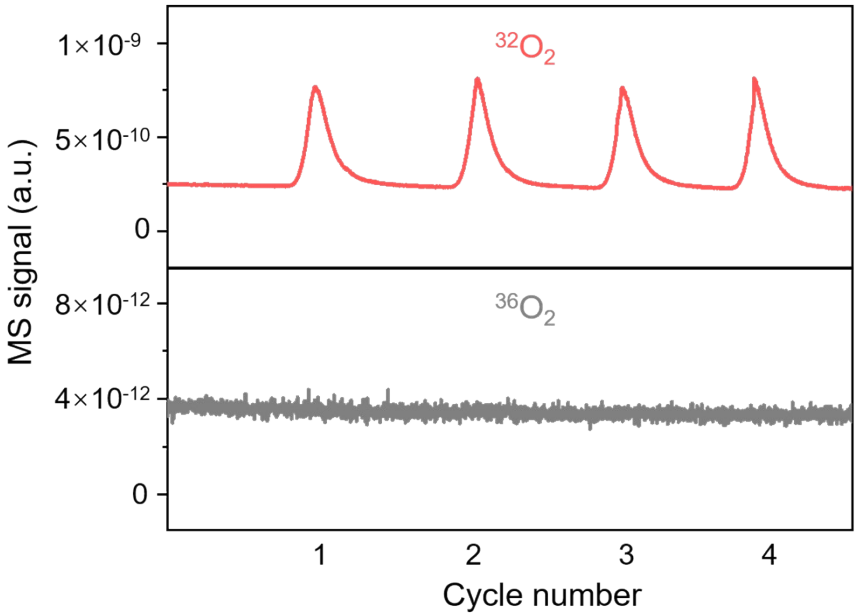

Figure S29. DEMS signals of O_2 products for CrO_2-0.16IrO_2 electrocatalyst. For the lattice oxygen mechanism (LOM)-type OER, the ^{18}O on neighboring Ir sites will have probability of coupling together to form $^{36}O_2$. Note that $^{36}O_2$ product signal was negligible as the OER proceeds while the signal of $^{32}O_2$ generates with each CV cycle in our experiments, suggesting the CrO_2-0.16IrO_2 electrocatalyst goes through an AEM-type OER process.

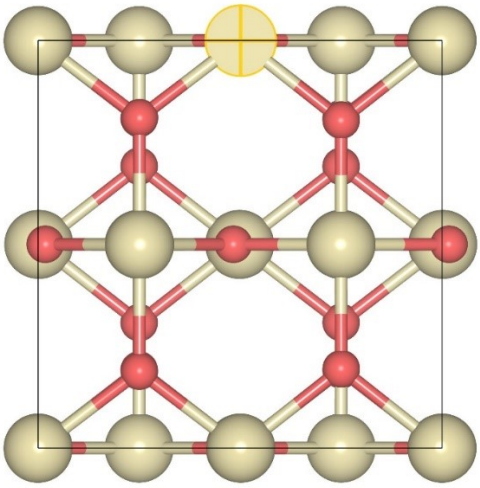

Figure S30. Simulated model of IrO_2 (110) plane. Gold and red balls represent Ir and O atoms.

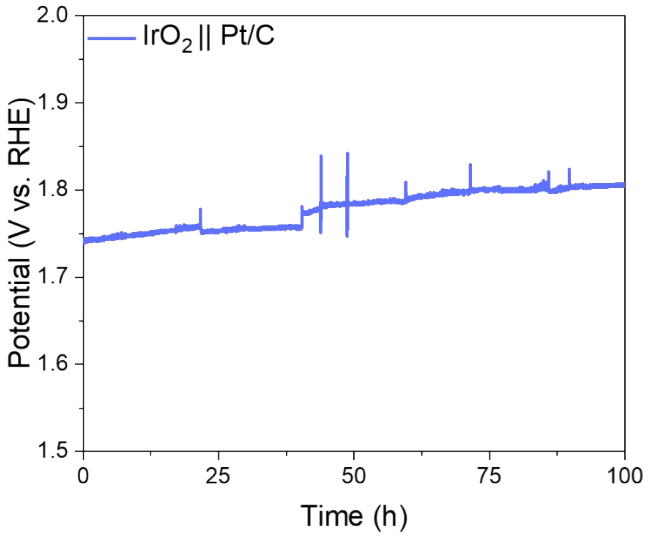

Figure S31. Chronopotentiometry test of the commercial IrO_2 electrocatalyst at 1 A cm^{-2} in the PEM electrolyzer. The degradation rate of commercial IrO_2 is 0.6 mV h^{-1}, which is higher than that of CrO_2-0.16IrO_2 electrocatalyst (0.5 mV h^{-1}). In addition, the Ir usage of CrO_2-0.16IrO_2 electrocatalyst is 0.59 mg cm^{-2}, while the amount of IrO_2 is 3.0 mg cm^{-2} in this test. Therefore, CrO_2-0.16IrO_2 electrocatalyst achieves higher activity and more stable operation with a low amount of iridium compared to commercial IrO_2.

Table S1. The masses of Cr and Ir elements in CrO_2-0.16IrO_2 determined by ICP-OES. The size of the test sample was 0.4 × 1 cm^2, and the mass of the test sample was 220.58 mg.

Element	Solution concentration (mg/L)	Element proportion (mg/kg)	Element mass (μg)	Element amount (μmol)
Cr	0.35	159	35	0.67
Ir	0.20	92	20	0.11

Note: The remaining sample mass belongs to Ti foil substrate.

Table S2. The dissolved mass of Ir from CrO_2-0.16IrO_2 and IrO_2 electrocatalysts during a chronopotentiometry test at 1,000 mA cm^{-2} determined by ICP-OES.

Time (h)	CrO_2-0.16IrO_2 (μg)	IrO_2 (μg)
10	7.7 ± 0.1	27.7 ± 0.6
20	7.8 ± 0.0	27.8 ± 0.0
30	8.0 ± 0.1	29.9 ± 0.2
40	8.1 ± 0.1	32.1 ± 0.1
50	8.2 ± 0.1	36.5 ± 0.1
60	8.2 ± 0.2	37.8 ± 0.1
70	8.2 ± 0.1	46.6 ± 0.5
80	8.3 ± 0.1	48.2 ± 0.2
90	8.6 ± 0.1	54.0 ± 0.4
100	8.8 ± 0.2	54.7 ± 0.6

Table S3. Comparison of mass loaded and corresponding mass activity for the CrO_2-0.16IrO_2 electrocatalyst and reported Ir-based catalysts in an acidic electrolyte at 25 °C.

Electrocatalyst	**Electrolyte**	**Mass activity @1.53 V vs. RHE (A g_{Ir}^{-1})**	**Loading mass (μg_{Ir} cm^{-2})**	**Refs.**
CrO_2-0.16IrO_2	0.5 M H_2SO_4	762 A g_{Ir}^{-1} @ 1.53 V	50	This work
IrO_2 nanoneedles	1 M H_2SO_4	55 A g_{Ir}^{-1} @ 1.53 V	250	[18]
6H-$SrIrO_3$	0.5 M H_2SO_4	75 A g_{Ir}^{-1} @ 1.53 V	52.7	[19]
La_2LiIrO_6	0.05 M H_2SO_4	40 A g_{Ir}^{-1} @ 1.53 V	250	[20]
Li-IrOx	0.5 M H_2SO_4	100 A g_{Ir}^{-1} @ 1.53 V	50	[21]
$Pr_2Ir_2O_7$	0.1 M $HClO_4$	424.5 A g_{Ir}^{-1} @ 1.53 V	28	[22]
Pt-Ir-Pd	0.1 M $HClO_4$	200 A g_{Ir}^{-1} @ 1.53 V	16.8	[23]
IrOx	0.05 M H_2SO_4	325 A g_{Ir}^{-1} @ 1.53 V	10.2	[24]
IrNiCu nanofram	0.1 M $HClO_4$	460 A g_{Ir}^{-1} @ 1.53 V	20	[25]
ATO/IrO_2	0.5 M H_2SO_4	63 A g_{Ir}^{-1} @ 1.53 V	50	[26]
IrNiOx/Meso-ATO	0.05 M H_2SO_4	90 A g_{Ir}^{-1} @ 1.51 V	10.2	[27]
P-$IrCu_{1.4}$	0.05 M H_2SO_4	220 A g_{Ir}^{-1} @ 1.55 V	60	[28]
Ru@IrO_x	0.05 M H_2SO_4	645 A g_{Ir}^{-1} @ 1.56 V	51	[29]
Li-$IrSe_2$	0.5 M H_2SO_4	66 A g_{Ir}^{-1} @ 1.45 V	150	[30]
Mesoporous Ir nanosheets	0.5 M H_2SO_4	260 A g_{Ir}^{-1} @ 1.45 V	136	[31]
SZIO	0.1 M $HClO_4$	1,540 A g_{Ir}^{-1} @ 1.53 V	41.5	[32]

Commercial IrO_2	0.1 M $HClO_4$	24 A g_{Ir}^{-1} @ 1.525 V	-	[33]
Commercial IrO_2	0.1 M $HClO_4$	12.6 A g_{Ir}^{-1} @ 1.53 V	-	[34]
Commercial IrO_2	0.5 M H_2SO_4	6 A g_{Ir}^{-1} @ 1.446V	-	[35]
Commercial IrO_2	0.5 M H_2SO_4	24.8 A g_{Ir}^{-1} @ 1.6V	2000	This work

Table S4. Comparison of the highest current density and the overpotentials at 200 mA cm^{-2} for the CrO_2-0.16IrO_2 electrocatalyst and reported OER electrocatalysts at 25 °C.

Electrocatalysts	**Electrolyte**	**Highest current density (mA cm^{-2})**	**η@200 mA cm^{-2} (mV)**	**Refs.**
CrO_2-0.16IrO_2	0.5 M H_2SO_4	2,000	353	This work
Ir-SA@Fe@NCNT	0.5 M H_2SO_4	276	470	[36]
Ir-$NiCo_2O_4$ NSs	0.5 M H_2SO_4	350	384	[37]
RuCo@CD	0.5 M H_2SO_4	200	470	[38]
Ir/GF	0.5 M H_2SO_4	300	430	[39]
CoMoNiS-NF-31	0.5 M H_2SO_4	200	385	[40]
Co-MoS_2-0.5	0.5 M H_2SO_4	250	430	[41]
Co_3O_4/CP	0.5 M H_2SO_4	200	358	[42]
Co_2MnO_4@FTO	0.5 M H_2SO_4	1,000	522	[43]
Co_2MnO_4@carbon plate	0.5 M H_2SO_4	1,000	492	[43]
Co_2MnO_4@Pt/Ti plate	0.5 M H_2SO_4	1,000	462	[43]
Co_2MnO_4/Pt-Ti mesh	0.5 M H_2SO_4	2,000	451	[43]
Ti/TiN@Co5.47N	0.1 M $HClO_4$	450	408	[44]

Table S5. Comparison of the overpotentials at 1,000, 1,500, and 2,000 mA cm^{-2} for the CrO_2-0.16IrO_2 electrocatalyst and reported OER electrocatalysts in a 0.5 M H_2SO_4 electrolyte at 25 °C.

Electrocatalysts	**Electrolyte**	**η @ 1,000 mA cm^{-2} (mV)**	**η @ 1,500 mA cm^{-2} (mV)**	**η @ 2,000 mA cm^{-2} (mV)**	**Refs.**
CrO_2-0.16IrO_2	0.5 M H_2SO_4	405	418	425	This work
W-Ir-B	0.5 M H_2SO_4	454	480	500	[45]
Co_2MnO_4	0.5 M H_2SO_4	550	597	632	[43]

Table S6. Summary of current density and stability test time of reported OER electrocatalysts at current densities ≤ 10 mA cm^{-2} at 25 °C.

Electrocatalysts	Electrolyte	Test current density (mA cm^{-2})	Time (h)	Refs.
Cu-doped RuO_2	0.5 M H_2SO_4	10	8	[46]
$W_{0.09}Ir_{0.01}O_{3-\sigma}$	1.0 M H_2SO_4	10	0.56	[47]
P-$IrCu_{1.4}$NCs	0.05 M H_2SO_4	10	10	[28]
IrNi NCs	0.1 M $HClO_4$	5	2	[48]
Ru_1-Pt_3Cu	0.1 M $HClO_4$	10	28	[49]
Co-RuIr	0.1 M $HClO_4$	10	25	[50]
Co doped RuO_2	0.5 M H_2SO_4	10	25	[51]
$Cr_{0.6}Ru_{0.4}O_2$	0.5 M H_2SO_4	10	10	[52]
6H-$SrIrO_3$	0.5 M H_2SO_4	10	30	[19]
IrO_x/$SrIrO_3$	0.5 M H_2SO_4	10	30	[53]
$SrTi_{0.67}Ir_{0.33}O_3$	0.1 M $HClO_4$	10	20	[33]
$CaCu_3Ru_4O_{12}$	0.5 M H_2SO_4	10	24	[54]
$Y_2Ir_2O_7$	0.1 M $HClO_4$	10	24	[55]
$Ru_1Ir_1O_x$	0.5 M H_2SO_4	10	110	[56]
$Ir_{0.06}Co_{2.94}O_4$	0.1 M $HClO_4$	10	200	[57]
SS Pt-RuO_2	0.5 M H_2SO_4	10	100	[58]
C-RuO_2-RuSe-10	0.5 M H_2SO_4	10	50	[59]
RuIr@CoNC	0.5 M H_2SO_4	10	40	[60]
IrNi-LY	0.1 M $HClO_4$	10	2	[61]
Mesoporous Ir nanosheets	0.5 M H_2SO_4	10	8	[31]
Ir_6Ag_9 nanotubes	0.5 M H_2SO_4	5	6	[62]
$Ir_{44}Pd_{19}$ nanocages	0.1 M $HClO_4$	10	15	[63]

$Ir_{0.6}Cr_{0.4}O_x$ nanowires	0.5 M H_2SO_4	10	25	[64]
Ir-SA@Fe@NCNT	0.5 M H_2SO_4	10	11.5	[36]
Co_3O_4/FTO	0.5 M H_2SO_4	10	12	[65]
γ-MnO_2/FTO	1.0 M H_2SO_4	10	8000	[66]
NiFeP	0.5 M H_2SO_4	10	30	[67]
$Mn_{7.5}O_{10}Br_3$	0.5 M H_2SO_4	10	500	[68]
Co/CoP	0.5 M H_2SO_4	1	12	[69]
TiB_2/FTO	1.0 M $HClO_4$	10	10	[70]

Table S7. Comparison of test current density, test time and corresponding degradation rate for the CrO_2-0.16IrO_2 electrocatalyst and reported OER electrocatalysts in a 0.5 M H_2SO_4 electrolyte at 25 °C.

Electrocatalysts	**Test current density (mA cm^{-2})**	**Time (h)**	**Degradation rate (mV h^{-1})**	**Refs.**
CrO_2-0.16IrO_2	1000	100	0.51	This work
C-RuO_2-RuSe-0.5	20	50	1.20	[59]
C-RuO_2-RuSe-0.5	50	50	1.84	[59]
Co_3O_4@C/CP	100	86.9	2.84	[42]
$Ru_1Ir_1O_x$	100	110	0.20	[56]
Ir-MoO_3	100	48	2.08	[71]
H-Ti@IrO_x	200	130	1.15	[72]
Co_2MnO_4	200	60	5.70	[43]

Table S8. Comparison of the cell voltage at 2 A cm^{-2} for the CrO_2-0.16IrO_2 electrocatalyst and reported Ir-based electrocatalysts in a PEM electrolyzer.

Electrocatalysts	**Current density (A cm^{-2})**	**Cell voltage (V)**	**Electrolyte**	**Test temperature (°C)**	**Refs.**
CrO_2-0.16IrO_2	2	1.73	H_2O	80	This work
GB-$Ta_{0.1}Tm_{0.1}Ir_{0.8}O_{2-\delta}$	2	1.81	0.5 M H_2SO_4	50	[73]
npIr_x-NS	2	1.86	H_2O	80	[74]
Ir-PTL	2	1.93	H_2O	80	[75]
Ir@WOxNRs-10	2	1.96	H_2O	80	[76]

References

1. Y. Lin, Q. Yan, C. Kong and L. Chen, *Sci Rep*, 2013, **3**, 1859.
2. P. Hohenberg and W. Kohn, *Phys Rev*, 1964, **136**, B864-B871.
3. G. Kresse and J. Hafner, *Phys Rev B Condens Matter*, 1994, **49**, 14251-14269.
4. G. Kresse and J. Furthmüller, *Phys Rev B*, 1996, **54**, 11169-11186.
5. G. Kresse and J. Furthmüller, *Computational Materials Sci*, 1996, **6**, 15-50.
6. P. E. Blochl, *Phys Rev B Condens Matter*, 1994, **50**, 17953-17979.
7. J. P. Perdew, K. Burke and M. Ernzerhof, *Phys Rev Lett*, 1996, **77**, 3865-3868.
8. H. Bendaoud, K. O. Obodo and B. Bouhafs, *Computational Condensed Matter*, 2019, **21**, e00400.
9. A. Smolyanyuk, M. Aichhorn, I. I. Mazin and L. Boeri, *Phys Review B*, 2019, **100**, 235114.
10. H. J. Monkhorst and J. D. Pack, *Phys Rev B*, 1976, **13**, 5188-5192.
11. J. G. Ángyán, I. C. Gerber, A. Savin and J. Toulouse, *Phys Rev A*, 2005, **72**, 012510.
12. J. K. Nørskov, J. Rossmeisl, A. Logadottir, L. Lindqvist, J. R. Kitchin, T. Bligaard and H. Jónsson, *J Phys Chem B*, 2004, **108**, 17886-17892.
13. G.-L. Chai, K. Qiu, M. Qiao, M.-M. Titirici, C. Shang and Z. Guo, *Energy Environ Sci*, 2017, **10**, 1186-1195.
14. Z. Pavlovic, C. Ranjan, Q. Gao, M. van Gastel and R. Schlögl, *ACS Catal*, 2016, **6**, 8098-8105.
15. M. Mohammadtaheri, Q. Yang, Y. Li and J. Corona-Gomez, *Coatings*, 2018, **8**, 111.
16. C. Aguilera, J. C. González, A. Borrás, D. Margineda, J. M. González, A. R. González-Elipe and J. P. Espinós, *Thin Solid Films*, 2013, **539**, 1-11.
17. Y. Luo, Z. Zhang, F. Yang, J. Li, Z. Liu, W. Ren, S. Zhang and B. Liu, *Energy Environ Sci*, 2021, **14**, 4610-4619.
18. J. Lim, D. Park, S. S. Jeon, C.-W. Roh, J. Choi, D. Yoon, M. Park, H. Jung and H. Lee, *Adv Funct Mater*, 2018, **28**, e1704796.
19. L. Yang, G. Yu, X. Ai, W. Yan, H. Duan, W. Chen, X. Li, T. Wang, C. Zhang, X. Huang, J. S. Chen and X. Zou, *Nat Commun*, 2018, **9**, 5236.
20. A. Grimaud, A. Demortière, M. Saubanère, W. Dachraoui, M. Duchamp, M.-L. Doublet and J.-M. Tarascon, *Nat Energy*, 2016, **2**, 1-10.
21. J. Gao, C. Q. Xu, S. F. Hung, W. Liu, W. Cai, Z. Zeng, C. Jia, H. M. Chen, H. Xiao, J. Li, Y. Huang and B. Liu, *J Am Chem Soc*, 2019, **141**, 3014-3023.
22. C. Shang, C. Cao, D. Yu, Y. Yan, Y. Lin, H. Li, T. Zheng, X. Yan, W. Yu, S. Zhou and J. Zeng, *Adv Mater*, 2019, **31**, e1805104.
23. J. Zhu, M. Xie, Z. Chen, Z. Lyu, M. Chi, W. Jin and Y. Xia, *Adv Energy Mater*, 2020, **10**, e1904114.
24. H. N. Nong, T. Reier, H.-S. Oh, M. Gliech, P. Paciok, T. H. T. Vu, D. Teschner,

M. Heggen, V. Petkov, R. Schlögl, T. Jones and P. Strasser, *Nat Catal*, 2018, **1**, 841-851.
25. J. Park, Y. J. Sa, H. Baik, T. Kwon, S. H. Joo and K. Lee, *ACS Nano*, 2017, **11**, 5500-5509.
26. D. Böhm, M. Beetz, M. Schuster, K. Peters, A. G. Hufnagel, M. Döblinger, B. Böller, T. Bein and D. Fattakhova-Rohlfing, *Adv Funct Mater*, 2019, **30**, e1906670.
27. H. N. Nong, H. S. Oh, T. Reier, E. Willinger, M. G. Willinger, V. Petkov, D. Teschner and P. Strasser, *Angew Chem Int Ed Engl*, 2015, **54**, 2975-2979.
28. Y. Pi, J. Guo, Q. Shao and X. Huang, *Chem Mater*, 2018, **30**, 8571-8578.
29. J. Shan, C. Guo, Y. Zhu, S. Chen, L. Song, M. Jaroniec, Y. Zheng and S.-Z. Qiao, *Chem*, 2019, **5**, 445-459.
30. T. Zheng, C. Shang, Z. He, X. Wang, C. Cao, H. Li, R. Si, B. Pan, S. Zhou and J. Zeng, *Angew Chem Int Ed Engl*, 2019, **58**, 14764-14769.
31. B. Jiang, Y. Guo, J. Kim, A. E. Whitten, K. Wood, K. Kani, A. E. Rowan, J. Henzie and Y. Yamauchi, *J Am Chem Soc*, 2018, **140**, 12434-12441.
32. X. Liang, L. Shi, R. Cao, G. Wan, W. Yan, H. Chen, Y. Liu and X. Zou, *Adv Mater*, 2020, **32**, e2001430.
33. X. Liang, L. Shi, Y. Liu, H. Chen, R. Si, W. Yan, Q. Zhang, G. D. Li, L. Yang and X. Zou, *Angew Chem Int Ed Engl*, 2019, **58**, 7631-7635.
34. G. Wu, X. Zheng, P. Cui, H. Jiang, X. Wang, Y. Qu, W. Chen, Y. Lin, H. Li, X. Han, Y. Hu, P. Liu, Q. Zhang, J. Ge, Y. Yao, R. Sun, Y. Wu, L. Gu, X. Hong and Y. Li, *Nat Commun*, 2019, **10**, 4855.
35. H. Su, W. Zhou, W. Zhou, Y. Li, L. Zheng, H. Zhang, M. Liu, X. Zhang, X. Sun, Y. Xu, F. Hu, J. Zhang, T. Hu, Q. Liu and S. Wei, *Nat Commun*, 2021, **12**, 6118.
36. F. Luo, H. Hu, X. Zhao, Z. Yang, Q. Zhang, J. Xu, T. Kaneko, Y. Yoshida, C. Zhu and W. Cai, *Nano Lett*, 2020, **20**, 2120-2128.
37. J. Yin, J. Jin, M. Lu, B. Huang, H. Zhang, Y. Peng, P. Xi and C. H. Yan, *J Am Chem Soc*, 2020, **142**, 18378-18386.
38. T. Feng, G. Yu, S. Tao, S. Zhu, R. Ku, R. Zhang, Q. Zeng, M. Yang, Y. Chen, W. Chen, W. Chen and B. Yang, *J Mater Chem A*, 2020, **8**, 9638-9645.
39. J. Zhang, G. Wang, Z. Liao, P. Zhang, F. Wang, X. Zhuang, E. Zschech and X. Feng, *Nano Energy*, 2017, **40**, 27-33.
40. Y. Yang, H. Yao, Z. Yu, S. M. Islam, H. He, M. Yuan, Y. Yue, K. Xu, W. Hao, G. Sun, H. Li, S. Ma, P. Zapol and M. G. Kanatzidis, *J Am Chem Soc*, 2019, **141**, 10417-10430.
41. Q. Xiong, X. Zhang, H. Wang, G. Liu, G. Wang, H. Zhang and H. Zhao, *Chem Commun*, 2018, **54**, 3859-3862.
42. X. Yang, H. Li, A.-Y. Lu, S. Min, Z. Idriss, M. N. Hedhili, K.-W. Huang, H. Idriss and L.-J. Li, *Nano Energy*, 2016, **25**, 42-50.
43. A. Li, S. Kong, C. Guo, H. Ooka, K. Adachi, D. Hashizume, Q. Jiang, H. Han, J. Xiao and R. Nakamura, *Nat Catal*, 2022, **5**, 109-118.
44. D. Guo, Z. Wan, Y. Li, B. Xi and C. Wang, *Adv Funct Mater*, 2020, **31**, e2008511.

45. R. Li, H. Wang, F. Hu, K. C. Chan, X. Liu, Z. Lu, J. Wang, Z. Li, L. Zeng, Y. Li, X. Wu and Y. Xiong, *Nat Commun*, 2021, **12**, 3540.
46. J. Su, R. Ge, K. Jiang, Y. Dong, F. Hao, Z. Tian, G. Chen and L. Chen, *Adv Mater*, 2018, **30**, e1801351.
47. S. Kumari, B. P. Ajayi, B. Kumar, J. B. Jasinski, M. K. Sunkara and J. M. Spurgeon, *Energy Environ Sci*, 2017, **10**, 2432-2440.
48. Y. Pi, Q. Shao, P. Wang, J. Guo and X. Huang, *Adv Funct Mater*, 2017, **27**, e1700886.
49. Y. Yao, S. Hu, W. Chen, Z.-Q. Huang, W. Wei, T. Yao, R. Liu, K. Zang, X. Wang, G. Wu, W. Yuan, T. Yuan, B. Zhu, W. Liu, Z. Li, D. He, Z. Xue, Y. Wang, X. Zheng, J. Dong, C.-R. Chang, Y. Chen, X. Hong, J. Luo, S. Wei, W.-X. Li, P. Strasser, Y. Wu and Y. Li, *Nat Catal*, 2019, **2**, 304-313.
50. J. Shan, T. Ling, K. Davey, Y. Zheng and S. Z. Qiao, *Adv Mater*, 2019, **31**, e1900510.
51. J. Wang, Y. Ji, R. Yin, Y. Li, Q. Shao and X. Huang, *J Mater Chem A*, 2019, **7**, 6411-6416.
52. Y. Lin, Z. Tian, L. Zhang, J. Ma, Z. Jiang, B. J. Deibert, R. Ge and L. Chen, *Nat Commun*, 2019, **10**, 162.
53. L. C. Seitz, C. F. Dickens, K. Nishio, Y. Hikita, J. Montoya, A. Doyle, C. Kirk, A. Vojvodic, H. Y. Hwang, J. K. Norskov, T. F. Jaramillo, *Science* 2016, **353**, 1011.
54. X. Miao, L. Zhang, L. Wu, Z. Hu, L. Shi and S. Zhou, *Nat Commun*, 2019, **10**, 3809.
55. P.-C. Shih, J. Kim, C.-J. Sun and H. Yang, *ACS Appl Energy Mater*, 2018, **1**, 3992-3998.
56. J. He, X. Zhou, P. Xu and J. Sun, *Adv Energy Mater*, 2021, **11**, e2102883.
57. J. Shan, C. Ye, S. Chen, T. Sun, Y. Jiao, L. Liu, C. Zhu, L. Song, Y. Han, M. Jaroniec, Y. Zhu, Y. Zheng and S. Z. Qiao, *J Am Chem Soc*, 2021, **143**, 5201-5211.
58. J. Wang, H. Yang, F. Li, L. Li, J. Wu, S. Liu, T. Cheng, Y. Xu, Q. Shao, X. Huang, *Sci Adv*, 2022, **8**, eabl9271.
59. J. Wang, C. Cheng, Q. Yuan, H. Yang, F. Meng, Q. Zhang, L. Gu, J. Cao, L. Li, S.-C. Haw, Q. Shao, L. Zhang, T. Cheng, F. Jiao and X. Huang, *Chem*, 2022, **8**, 1673-1687.
60. J. Xu, J. Li, Z. Lian, A. Araujo, Y. Li, B. Wei, Z. Yu, O. Bondarchuk, I. Amorim, V. Tileli, B. Li and L. Liu, *ACS Catal*, 2021, **11**, 3402-3413.
61. J. Ruiz Esquius, G. Algara-Siller, I. Spanos, S. J. Freakley, R. Schlögl and G. J. Hutchings, *ACS Catal*, 2020, **10**, 14640-14648.
62. M. Zhu, Q. Shao, Y. Qian and X. Huang, *Nano Energy*, 2019, **56**, 330-337.
63. J. Zhu, Z. Chen, M. Xie, Z. Lyu, M. Chi, M. Mavrikakis, W. Jin and Y. Xia, *Angew Chem Int Ed Engl*, 2019, **58**, 7244-7248.
64. W. Gou, M. Zhang, Y. Zou, X. Zhou and Y. Qu, *ChemCatChem*, 2019, **11**, 6008-6014.
65. J. S. Mondschein, J. F. Callejas, C. G. Read, J. Y. C. Chen, C. F. Holder, C. K.

Badding and R. E. Schaak, *Chem Mater*, 2017, **29**, 950-957.
66. A. Li, H. Ooka, N. Bonnet, T. Hayashi, Y. Sun, Q. Jiang, C. Li, H. Han and R. Nakamura, *Angew Chem Int Ed Engl*, 2019, **58**, 5054-5058.
67. F. Hu, S. Zhu, S. Chen, Y. Li, L. Ma, T. Wu, Y. Zhang, C. Wang, C. Liu, X. Yang, L. Song, X. Yang and Y. Xiong, *Adv Mater*, 2017, **29**, e1606570.
68. S. Pan, H. Li, D. Liu, R. Huang, X. Pan, D. Ren, J. Li, M. Shakouri, Q. Zhang, M. Wang, C. Wei, L. Mai, B. Zhang, Y. Zhao, Z. Wang, M. Graetzel and X. Zhang, *Nat Commun*, 2022, **13**, 2294.
69. Z.-H. Xue, H. Su, Q.-Y. Yu, B. Zhang, H.-H. Wang, X.-H. Li and J.-S. Chen, *Adv Energy Mater*, 2017, **7**, e1602355.
70. M. J. Kirshenbaum, M. H. Richter and M. Dasog, *ChemCatChem*, 2019, **11**, 3877-3881.
71. X. Liu, S. Xi, H. Kim, A. Kumar, J. Lee, J. Wang, N. Q. Tran, T. Yang, X. Shao, M. Liang, M. G. Kim and H. Lee, *Nat Commun*, 2021, **12**, 5676.
72. Z. Yu, J. Xu, Y. Li, B. Wei, N. Zhang, Y. Li, O. Bondarchuk, H. Miao, A. Araujo, Z. Wang, J. L. Faria, Y. Liu and L. Liu, *J Mater Chem A*, 2020, **8**, 24743-24751.
73. S. Hao, H. Sheng, M. Liu, J. Huang, G. Zheng, F. Zhang, X. Liu, Z. Su, J. Hu, Y. Qian, L. Zhou, Y. He, B. Song, L. Lei, X. Zhang and S. Jin, *Nat Nanotechnol*, 2021, **16**, 1371-1377.
74. S. Chatterjee, X. Peng, S. Intikhab, G. Zeng, N. N. Kariuki, D. J. Myers, N. Danilovic and J. Snyder, *Adv Energy Mater*, 2021, **11**, e2101438.
75. X. Peng, P. Satjaritanun, Z. Taie, L. Wiles, A. Keane, C. Capuano, I. V. Zenyuk and N. Danilovic, *Adv Sci*, 2021, **8**, e2102950.
76. G. Jiang, H. Yu, Y. Li, D. Yao, J. Chi, S. Sun and Z. Shao, *ACS Appl Mater Interfaces*, 2021, **13**, 15073-15082.